**RESEARCH ARTICLE**

# On the role of transverse motion in pseudo-steady gravity currents

C. R. Marshall[1] · R. M. Dorrell[2] · G. M. Keevil[3] · J. Peakall[3] · S. M. Tobias[3]

## Abstract

Flow in the body of gravity currents is typically assumed to be statistically two-dimensional, and cross-stream flow is often neglected (Simpson 1997; Meiburg et al. 2015). Here, we assess the validity of such assumptions using Shake-the-Box particle tracking velocimetry measurements of experimental gravity current flows. The resulting instantaneous, volumetric, whole-field velocity measurements indicate that cross-stream and vertical velocities (and velocity fluctuations) are equivalent in magnitude and thus are key to energy distribution and dissipation within the flow. Further, the presented data highlight the limitations of basing conclusions regarding body structure on a single cross-stream plane (particularly if that plane is central). Spectral analysis and dynamic mode decomposition of the fully three-dimensional, volumetric velocity data suggests internal waves within the current body that are associated with coherent three-dimensional motions in higher Reynolds number flows. Additionally, a potential critical layer at the height of the downstream velocity maximum is identified.

## 1 Introduction

Gravity currents are flows driven by gravity, resulting from a density difference between the current and surrounding ambient fluids (Simpson 1997; Ungarish 2009). This density difference could be caused by, for example, the presence of a temperature difference, suspended sediment, or a solute. They are a common class of geophysical flow, with the potential to cause significant environmental damage, as well as being a key driver of global sediment transport (Simpson 1997; Kneller and Buckee 2000; Gray et al. 2006). Therefore, there has been significant experimental (Ellison and Turner 1959; Middleton 1966; Stacey and Bowen 1988; Hacker et al. 1996; Hallworth et al. 1996; Kneller et al. 1999; Gray et al. 2005) and numerical (Özgökmen et al. 2004; Cantero et al. 2007; Meiburg et al. 2015; Hogg et al. 2016) research into their structure and dynamics.

Gravity current flows can be divided into a head and a body (see Fig. 1). The majority of the existing research has focused on the head (Hacker et al. 1996; Hallworth et al. 1996; Middleton 1966; Islam and Imran 2010), despite the fact that the body often forms by far the largest part of the flow (Özsoy et al. 2001; Sumner et al. 2014; Azpiroz-Zabala et al. 2017), often persisting for hours (or days) or being quasi-permanent (Simpson 1997; Khripounoff et al. 2003; Parsons et al. 2007; Sumner et al. 2014; Peakall and Sumner 2015; Azpiroz-Zabala et al. 2017). Despite this, aspects of body flow remain poorly understood.

The gravity current body may be divided into two layers by the height of the velocity maximum (Altinakar et al. 1996; Dorrell et al. 2019; Wells and Dorrell 2021). The upper layer structure, determined by shear between the current and ambient fluids and by density stratification, has been described as similar to that in a wall-bounded jet, while the lower layer structure is similar to that of an open-channel flow (Altinakar et al. 1996; Kneller et al. 1999; Sequeiros et al. 2010). The body is often assumed to be statistically steady and two-dimensional, as observed by Simpson (1997), Meiburg et al. (2015), Kneller et al. (2016).

The validity of such assumptions has been questionable. Existing experimental work on the structure of the gravity current body has often been based on data from a single cross-stream plane (Kneller et al. 1997, 1999; Buckee et al. 2001; Gray et al. 2005; Cossu and Wells 2012). Additionally, while there have been attempts to quantify the magnitude of cross-stream motions within the gravity current body experimentally (Alahyari and Longmire 1994; Islam and Imran 2010; Krug et al. 2015; Lefauve et al. 2018; Neamtu-Halic et al. 2019), there are contradictory conclusions regarding

✉ G. M. Keevil
  g.m.keevil@leeds.ac.uk

[1] EPSRC Centre for Doctoral Training in Fluid Dynamics, University of Leeds, Leeds LS2 9JT, UK

[2] University of Hull, Hull HU6 7RX, UK

[3] University of Leeds, Leeds LS2 9JT, UK
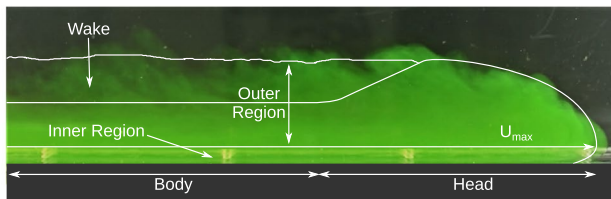
**Fig. 1** Flow visualisation from the work presented in this paper, overlaid by a gravity current structure as described by Kneller and Buckee (2000)

their magnitude and significance. Islam and Imran (2010), for example, suggest that cross-stream velocity should be considered (as it makes an equivalent contribution to turbulent kinetic energy as does vertical velocity), while Krug et al. (2015) conclude that cross-stream velocity is small and can be neglected. Whatever the source of the contradiction (for example, differences in flow parameters, spatial resolution, or position of the measurement region within the flow), there remain open questions relating to the nature and magnitude of cross-stream motions within the gravity current body.

Three-dimensional motions are known to exist in gravity currents. The numerical works of Espath et al. (2015) and Dai and Huang (2022), for example, highlight structures and three-dimensional motions within the head. In the gravity current body such motions may originate with, for example, the breakdown of Kelvin–Helmholtz structures behind the head (Lowe et al. 2002; Cantero et al. 2008; Balasubramanian and Zhong 2018; Pelmard et al. 2020), side-wall effects in cross-stream constrained flows [such as currents in submarine channels (Peakall and Sumner 2015)], or flow over three-dimensional bed forms (Paik et al. 2009; Nasr-Azadani and Meiburg 2014). The simulations of Salinas et al. (2021) identify three families of hairpin vortex within the body of supercritical gravity current flows (found near the bed, at the lower interface, and at the upper interface), with substantial impact on rate of entrainment. Additionally, in Marshall et al. (2021b, 2021a) large-scale wave-like motions (postulated to be internal gravity waves) were identified in two-dimensional PIV measurements and three-dimensional numerical simulations of gravity current flows. Further, in Marshall et al. (2021b) it was suggested that these waves may be forming a critical layer within the flow [a region where the mean flow speed is similar to the wave phase speed (Bühler 2014)].

Internal waves interacting with a critical layer could transfer momentum to the mean flow (Dorrell et al. 2019), causing local acceleration and questioning the assumption of a statistically steady flow. Further, wave breaking at a critical layer would reinforce an eddy transport barrier resulting from sharp density gradients across the

velocity maximum (Dorrell et al. 2019). This would in turn sharpen the density profile, and maintain the current/ambient interface over larger distances than previously thought. However, this eddy transport barrier cannot exist in a purely two-dimensional flow, instead requiring cross-stream flow and density variations (Dorrell et al. 2019). This highlights the importance of considering not only cross-stream velocity, but fully three-dimensional volumetric flow measurements.

In this paper, Shake-the-Box particle tracking velocimetry (Schanz et al. 2013, 2015, 2016; Tan et al. 2019) is used to generate instantaneous, whole-field, three-dimensional velocity measurements of a constant-influx gravity current. These measurements are used to discuss the three-dimensional nature of the current body, and to further quantify body structure. Specifically, the key aims are to assess whether: (i) neglecting cross-stream flow in the gravity current body is justifiable, (ii) any wave-like structures are present, (iii) any structures identified are associated with three-dimensional motions, and (iv) the nature of identified structures is affected by increased Reynolds number.

## 2 Methodology

### 2.1 The experimental setup

The experiments in this work consist of constant-influx, solute-based gravity current flows in a tank 0.1m wide, 0.2m deep, and 2m long (see schematic in Fig. 2). The raised sections at either end capture air entrained through the inlet or outlet, and the 0.5m drop above the outlet prolongs the body section of the flow by slowing the rate of current fluid pollution into the ambient fluid. In order to prevent the formation of bubbles on the lid of the tank, the bed slope is set to 0.1°. Initially, the tank is filled with ambient fluid (a 6% by mass solution of glycerol (GLY)). Dense fluid (a 6% by mass solution of potassium dihydrogen phosphate (KDP)) is then pumped in through the inlet at a constant rate using a positive-displacement gear pump to provide a steady inflow with an inverter to control the flow rate. A coarse mesh, with holes of diameter 7.8mm, is fitted over the inlet to provide a homogeneous inflow. Before entering the tank, the dense fluid passes through a bubble trap (a 1m long, 0.1m diameter cylinder mostly filled with dense fluid but with an air gap at the top) to remove air entrained by the gear pump. The airtight design results in fluid flowing through the outlet at the same rate that it is pumped through the inlet by the gear pump. Black aluminium polyethylene composite panels are used to cover the back and top of the tank to improve the image quality.

**Fig. 2** Schematic of the STB setup
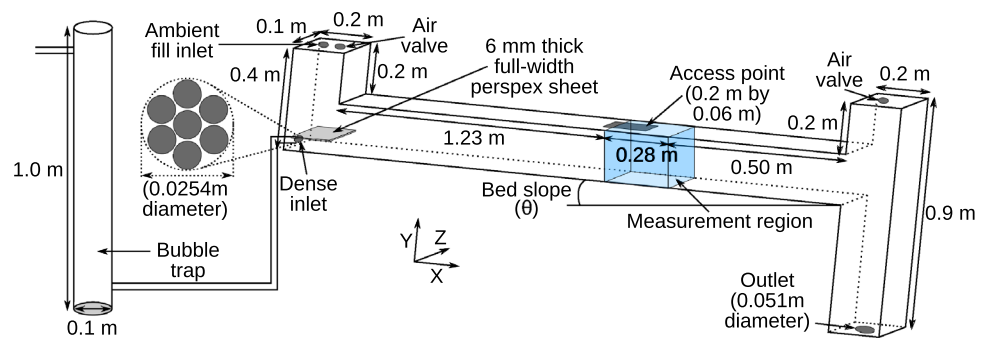


**Table 1** Details of the density, $\rho$, kinematic viscosity, $v$, and refractive index, $n$, of 6% by mass solutions of ambient (glycerol) and dense (potassium dihydrogen phosphate) solutes in tap water at 20°, from Haynes (2014)

|  | $\rho$ (kg m$^{-3}$) | $v$ (m$^2$s$^{-1}$) | $n$ |
|---|---|---|---|
| Glycerol (ambient fluid) | 1012.0 | $1.14 \times 10^{-6}$ | 1.3400 |
| Potassium dihydrogen phosphate (current fluid) | 1041.4 | $1.09 \times 10^{-6}$ | 1.3400 |

**Table 2** Details of the average particle diameter, $d_p$, density, $\rho$, concentration of seeding used in each fluid (GLY/KDP), and estimates of Stokes velocity ($U_g$), and relaxation time ($\tau_r$) for the seeding particles used (fluorescent Cospheric polyethylene microspheres UVPMS-BO−1.00)

|  | $d_p$ (µm) | $\rho$ (kg m$^{-3}$) | Concentration (g L$^{-1}$) | $U_g$ (m s$^{-1}$) | $\tau_r$ (s) |
|---|---|---|---|---|---|
| Seeding | 138 | 1000 | 0.020/0.033 | $3 \times 10^{-4}$ | $9.2 \times 10^{-4}$ |

## 2.2 Refractive index matching

The experimental fluids, which have a density difference of 3% (see Table 1), are mixed in two 150L mixing tanks. The two fluids, as well as a mixture of the two, are refractive index matched as required for optical techniques such as PIV and STB (Alahyari and Longmire 1994). The density and refractive index of each fluid are tested using both a Reichert AR200 digital refractometer and an Anton Paar DMA$^{TM}$ 35 Basic density meter, and the temperature is monitored. To be deemed refractive index matched, the fluids are required to be equal to the value in Table 1 to the precision of the refractometer (5 significant figures) and consistent across 3 readings at least 5 min apart. While temperature differences result in variations, density was always within the range $1012.9 \pm 0.1$ kg m$^{-3}$ for the glycerol solution and $1041.5 \pm 0.5$ kg m$^{-3}$ for the KDP. Selecting a single pair of refractive index matched fluids ensures that the viscosity is as similar as possible between cases; however, the depth-averaged Froude number is restricted to sub-critical flow.

## 2.3 The Shake-the-Box system

Shake-the-Box particle tracking velocimetry (STB) is used to generate instantaneous three-dimensional volumetric measurements of velocity (Schanz et al. 2016; Wieneke 2012). This method consists of adding seeding particles to the flow, and repeatedly photographing an illuminated volume at a known time interval using a synchronised array of cameras with overlapping fields of view. Particle positions

are reconstructed using triangulation and by extrapolation of particle tracks identified from previous timesteps.

The seeding particles used in this work are fluorescent Cospheric polyethylene microspheres UVPMS-BO−1.00 (Fl). Table 2 includes details of these particles, the concentrations used in this work, and estimates of the Stokes velocity and relaxation times for the particles demonstrating that they are suitable for use as seeding in these experiments.

A volume within the flow is illuminated using a LaVision Blue LED-Flashlight 300. The images are captured using a LaVision MiniShaker TR-L that captures 0.275m horizontally, 0.15m vertically, and to within 5mm of the side walls. The location of this measurement volume is shown in Fig. 2. A filter with a cut-off at wavelength 610nm is applied to each camera to reduce the effect of reflections from the perspex walls.

Image collection begins several seconds before the current head reaches the measurement region. Data collection is limited by the RAM capacity of the acquisition computer. The duration of measurement is therefore restricted to either 25s or 50s depending on whether image collection is at 100Hz or 50Hz (see Table 3), requiring $\mathcal{O}(10\text{GB})$ RAM. The binned velocity field is on a grid with spatial resolution 2.6mm × 2.6mm × 2.6mm. Image calibration is done using a LaVision 106-10 double-sided calibration plate on the bottom surface of the tank in a central cross-stream location and approximately central within the measurement region in the downstream direction. The three-dimensional velocity field is reconstructed using the STB algorithm in LaVision DaVis 10.0.5 and 10.1.0.

## 2.4 The experimental cases

A series of experiments are conducted to establish the effect of Reynolds number on the three-dimensional structure of the gravity current body. These cases cover a range of influx values ($Q$) determined by the pump. The lowest and highest influx cases are dictated by the minimum ($Q = 0.032$L s$^{-1}$) and maximum ($Q = 0.148$L s$^{-1}$) stable settings of the pump, with a third intermediate value ($Q = 0.082$L s$^{-1}$). The details of the influx and collection frequency for each STB case are shown in Table 3. For each case, a Reynolds and densimetric Froude number can be calculated based on characteristic velocity and length scales. As in Marshall et al. (2021b), these characteristic scales are calculated based on averaged profiles from the body of the flow.

Body data are defined as in Marshall et al. (2021b) by measuring the time taken for the current front to cross the measurement region, and then waiting that length of time again before averaging over downstream locations and time. For all cases in this work, this definition leads to consistent downstream velocity averages whether calculated over 5s or 20s suggesting that the data are approximately quasi-steady. Profiles of downstream velocity averaged over all downstream locations and time within the body are shown in Fig. 3. Except for the lowest Reynolds number case (which has positive flow in the ambient, possibly as a result of an air valve not being fully closed), all cases have the same averaged structure. Vertical location is non-dimensionalised by subtracting the average height of the velocity maximum and dividing by the Ellison and Turner integral length scale ($L_c$), and downstream velocity by dividing by maximum average downstream velocity ($U_c$),

**Table 3** Details of the influx and time between images for each STB case

| Case | 1 | 2 | 3 |
|---|---|---|---|
| Influx (L s$^{-1}$) | 0.032 | 0.082 | 0.148 |
| $\Delta t$ (m s$^{-1}$) | 20 | 10 | 10 |

$$Y^* = \frac{Y - Y_{\overline{U}_{max}}}{L_c},\ X^* = \frac{X}{L_c},\ Z^* = \frac{Z}{L_c},$$
$$U^* = \frac{U}{U_c},\ V^* = \frac{V}{U_c},\ W^* = \frac{W}{U_c},$$
$$L_c = \frac{\left(\int \bar{\bar{U}} dy\right)^2}{\int \bar{\bar{U}}^2 dy},$$
$$U_c = \overline{U}_{max}$$

(1)

(where $L$ is the height of the tank, and $\bar{\bar{U}}$ is the mean velocity relative to that in the ambient). This non-dimensionalisation collapses the downstream velocity profiles, and therefore, $L_c$ and $U_c$ are considered suitable characteristic length and velocity scales for calculation of Reynolds number ($\text{Re} = U_c L_c / \nu$) and densimetric Froude number ($Fr_D = U_c / \sqrt{g' L_c}$, where $g'$ is the reduced gravity). Note that the Ellison and Turner length scale is different from the current height, which is defined to be where the averaged downstream velocity $\bar{U} = 0$. As the kinematic viscosities of the experimental fluids are similar, the viscosity of the dense fluid was used for calculation of flow Reynolds number. A characteristic time scale can also be defined from the characteristic length and velocity scales, $t_c = L_c / U_c$. The Reynolds and Froude numbers resulting from these characteristic

**Fig. 3** **a** Downstream velocity and **b** non-dimensional downstream velocity, averaged over all downstream locations and body timesteps on a central $Z^* = 0$ plane



(a)

(b)
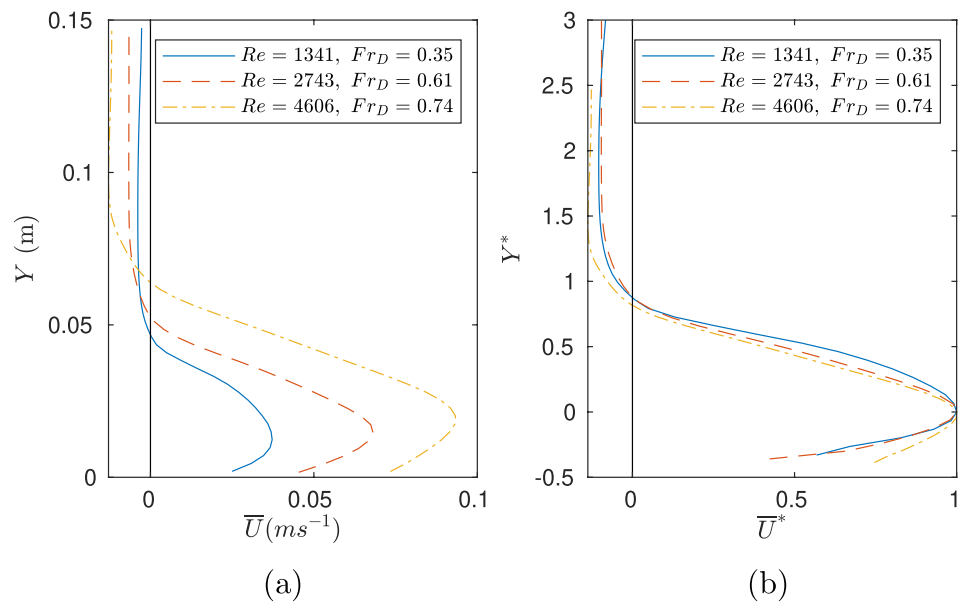
**Table 4** Characteristic velocity, $U_c = \overline{U}_{max}$, length, $L_c$, and time, $t_c$, scales, along with the Reynolds, $Re = U_c L_c / \nu$, and densimetric Froude, $Fr_D = U_c / \sqrt{g' L_c}$ numbers for each STB case

| Case | $U_c$ (m s$^{-1}$) | $L_c$ (m) | $t_c$ (s) | Re | $Fr_D$ |
|------|------|------|------|------|------|
| 1 | 0.037 | 0.039 | 1.06 | 1341 | 0.35 |
| 2 | 0.069 | 0.043 | 0.63 | 2743 | 0.61 |
| 3 | 0.093 | 0.054 | 0.58 | 4606 | 0.74 |

scales (shown in Table 4) are output parameters, for which a doubling of influx does not result in a doubling of Reynolds number.

# 3 Results

## 3.1 Flow on a central slice

Figures 4 and 5 show instantaneous plots of velocity ($U$, $V$, $W$) and velocity fluctuations from the mean ($U' = U - \overline{U}$, $V' = V - \overline{V}$, and $W' = W - \overline{W}$) at central cross-stream and downstream locations over time. In all cases, the vertical velocity has a similar structure of alternating positive/negative regions, though the magnitude of the velocity increases significantly with Reynolds number, as does the frequency of the motions. In the lowest Reynolds number case these regions are less well defined.

As well as the magnitude of cross-stream velocity increasing with increased Reynolds number, the structure changes. In the lowest Reynolds number case, cross-stream velocity takes the form of low magnitude bands. As Reynolds number increases, the structure becomes similar to that
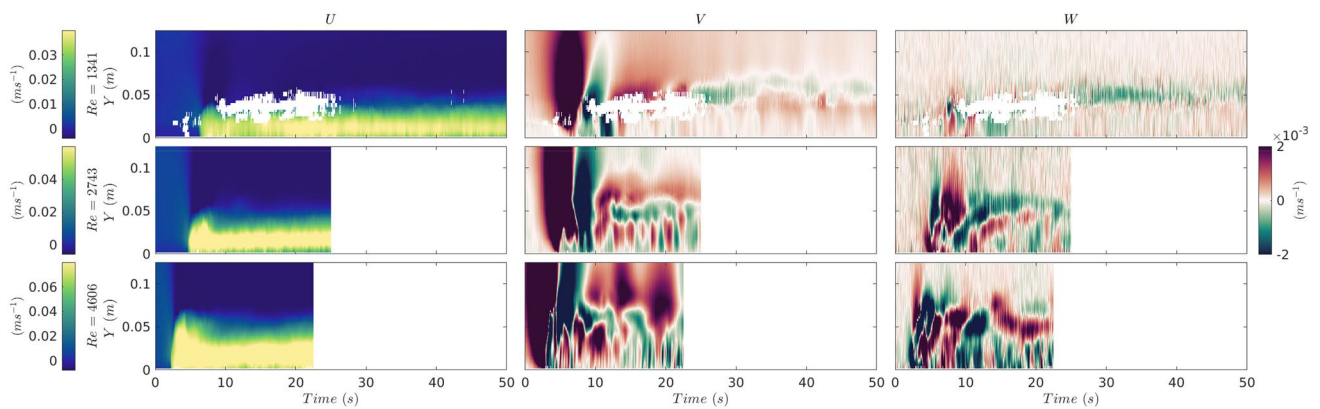


**Fig. 4** (left) Downstream, (middle) vertical, and (right) cross-stream velocities from the STB cases on a central cross-stream slice
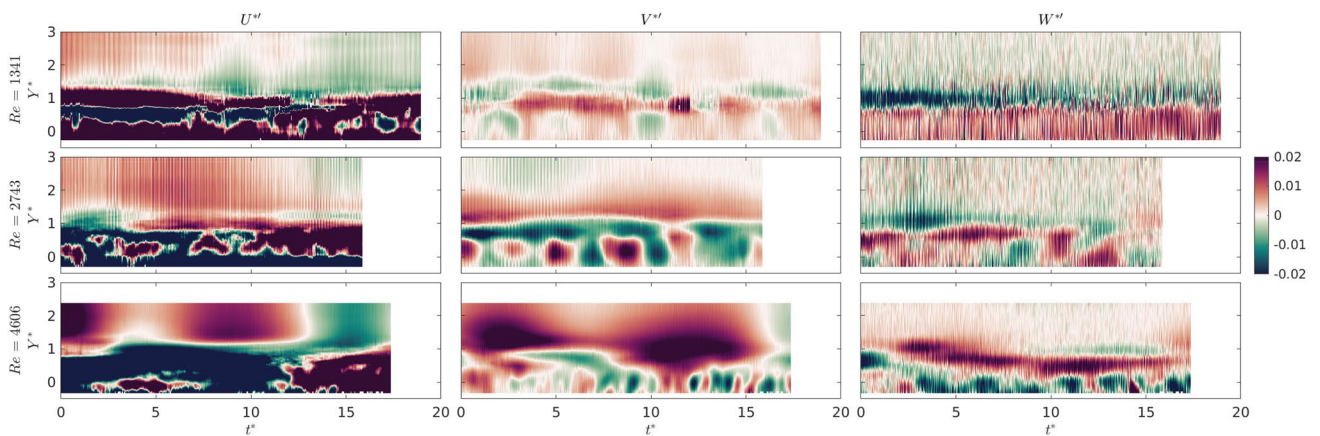


**Fig. 5** Instantaneous dimensionless fluctuations in (left) downstream (middle) vertical and (right) cross-stream velocities in the gravity current body from the STB cases on a central $Z^* = 0$ cross-stream slice

of the vertical velocity—alternating regions of positive and negative velocity. The pairs of cases with similar Reynolds number always have similar structure. Figure 5 demonstrates that in every case the magnitude of the cross-stream velocity fluctuations, $W'$, is equivalent to those in the vertical velocity, suggesting that it may not be reasonable to neglect cross-stream flow as often assumed (Simpson 1997; Meiburg et al. 2015).

Figure 6a shows the two-dimensional turbulent kinetic energies on this central slice,

$$k_{2D}^* = 0.5(U^{*\prime 2} + V^{*\prime 2}). \tag{2}$$

These averaged turbulent kinetic energies have a similar structure to those in the existing literature (Buckee et al. 2001; Gray et al. 2006; Islam and Imran 2010; Cossu and Wells 2012) and those presented in Marshall et al. (2021b), with a local minimum close to the velocity maximum and a local maximum between the velocity maximum and current height. In the highest Reynolds number cases, there is an additional local maximum just above the velocity maximum. The difference in magnitude between cases (for example, the low magnitude in the Re = 2743 case) may be linked to the time-dependent nature of the data, which can be seen in the instantaneous turbulent kinetic energy plots in Fig. 6b. The instantaneous turbulent kinetic energy is intermittent



(a)



(b)
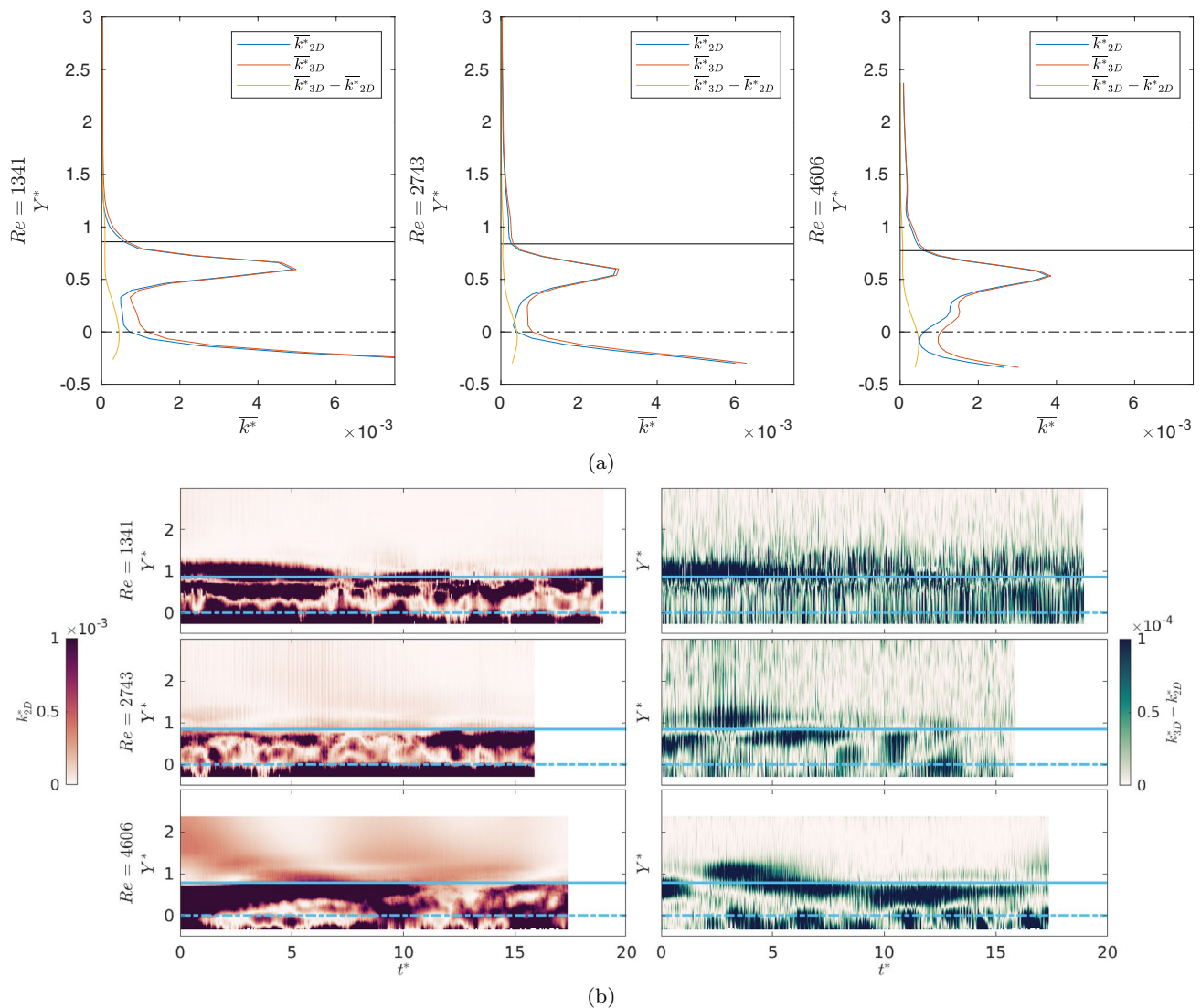
**Fig. 6** Plots of (**a**) $\overline{k_{2D}^*} = \overline{0.5(U^{*\prime 2} + V^{*\prime 2})}$, $\overline{k_{3D}^*} = \overline{0.5(U^{*\prime 2} + V^{*\prime 2} + W^{*\prime 2})}$, and $\overline{k_{3D}^*} - \overline{k_{2D}^*}$ on a central cross-stream slice (where $\overline{(\cdot)}$ indicates that the data are averaged over all downstream locations and body timesteps) for each of the STB cases, and (**b**) instantaneous (left) $k_{2D}^*$ and (right) $k_{3D}^* - k_{2D}^*$ data at a central downstream location over time. The solid horizontal line indicates the height of the current on the central cross-stream slice (defined as where downstream velocity changes from positive to negative), and the dot-dash line the height of the average velocity maximum on the central cross-stream slice

(particularly at higher Reynolds numbers) suggesting that averaging leads to a loss of information about the structure of the flow.

The three-dimensional velocity measurements presented allow consideration of the effect of cross-stream velocity on the calculation of turbulent kinetic energy,

$$k^*_{3D} = 0.5(U^{*\prime 2} + V^{*\prime 2} + W^{*\prime 2}). \tag{3}$$

Figure 6a shows the difference between the two- and three-dimensional calculations. The profiles have almost the same structure in every case—the biggest contributions being at the height of the velocity maximum (where the contribution from $W^{*\prime}$ is equivalent in magnitude to the contributions from $U^{*\prime}$ and $V^{*\prime}$), and a smaller increase at the current height. This hides some significant structural differences between cases (Fig. 6b). At the lowest Reynolds number, the contribution at the current height decreases over time, and that at the velocity maximum increases. However, the contributions are relatively consistent. As Reynolds number increases, the effect of cross-stream velocity at the velocity maximum becomes intermittent, and the contribution at the current height no longer decreases over time.

## 3.2 Alternative slices

Figure 7 shows downstream velocity, averaged over time and downstream locations, for a variety of cross-stream locations covering the central half of the tank. For all cases, moving towards the walls decreases the average magnitude of the downstream velocity of the flow as a result of wall drag. This effect is reduced as Reynolds number increases, with little difference between the central profile and that at $Z^* = 0.25$ for the highest Reynolds number case. This may be a result of greater variability in cross-stream velocity. Figure 8 shows velocity fluctuations at $Z^* = 0.5$ and a central

downstream location over time. Compared with Fig. 5, the velocity fluctuations have broadly similar structure and amplitude regardless of the plane considered for each case.

Figure 9 shows flow on X–Z planes over time at the height of maximum downstream velocity at a central downstream location, and the fluctuations from the mean calculated by averaging over all body timesteps. Again, these plots demonstrate that the magnitude of cross-stream and vertical velocities and velocity fluctuations are equivalent. As Reynolds number increases, there are significant changes in the velocity components. For the lowest Reynolds number case, the cross-stream velocity shows the fluid moving towards the centre of the measurement region at this height. There is a clear separation of positive and negative cross-stream velocities along a line close to the cross-stream centre. As Reynolds number increases, this separation breaks down, and the centreline has alternating positive/negative regions. By the highest Reynolds number case, the centreline is far less clear in the cross-stream velocity plots.

There are alternating regions of positive and negative vertical velocity in every case. However, as Reynolds number increases, their structure changes. In the lowest Reynolds number case, the negative vertical velocity motions are concentrated towards the side walls and are smaller in magnitude than the higher Reynolds number cases. Some of these do not extend across the full domain width. The intermediate Reynolds number case has alternating regions of positive and negative vertical velocity that are concentrated in the centre of the domain. In the highest Reynolds number case, these regions are smaller, less regular, and are not limited to the centreline.
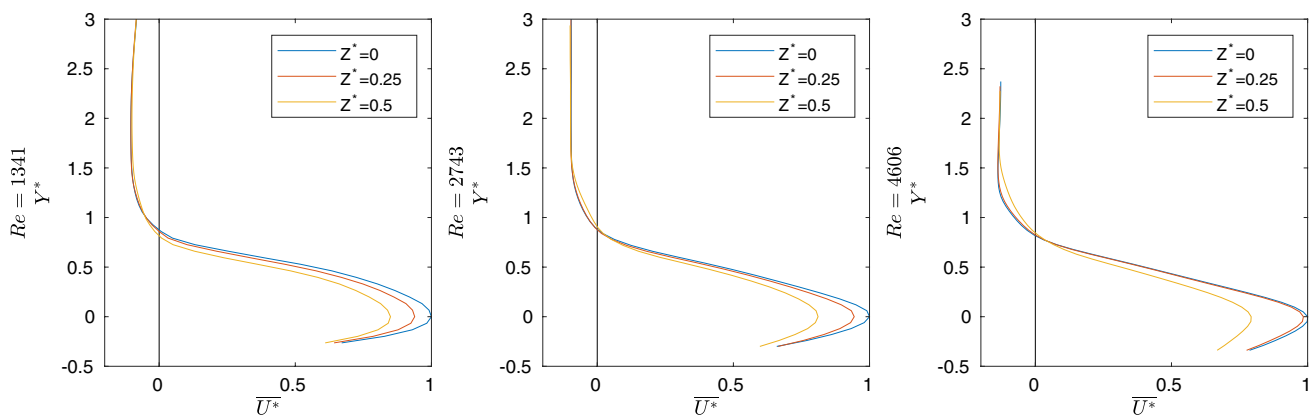


**Fig. 7** Comparisons of average downstream velocity profiles at a central downstream location averaged over all body timesteps for cross-stream locations $Z^* = 0$, 0.25 and 0.5
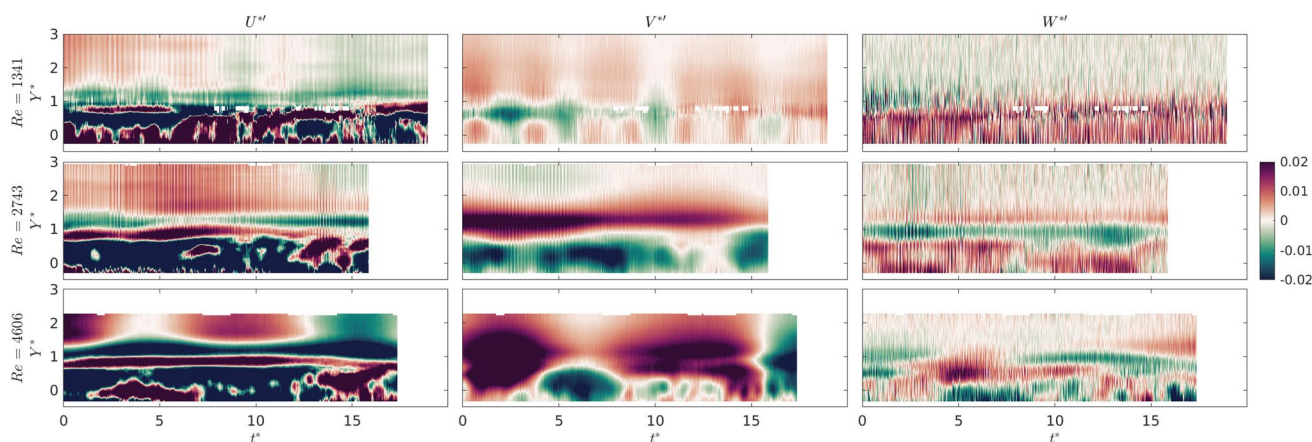
**Fig. 8** Velocity fluctuations (left) $U^{*\prime}$, (centre) $V^{*\prime}$, and (right) $W^{*\prime}$ at $Z^* = 0.5$, for each case at a central downstream location over time
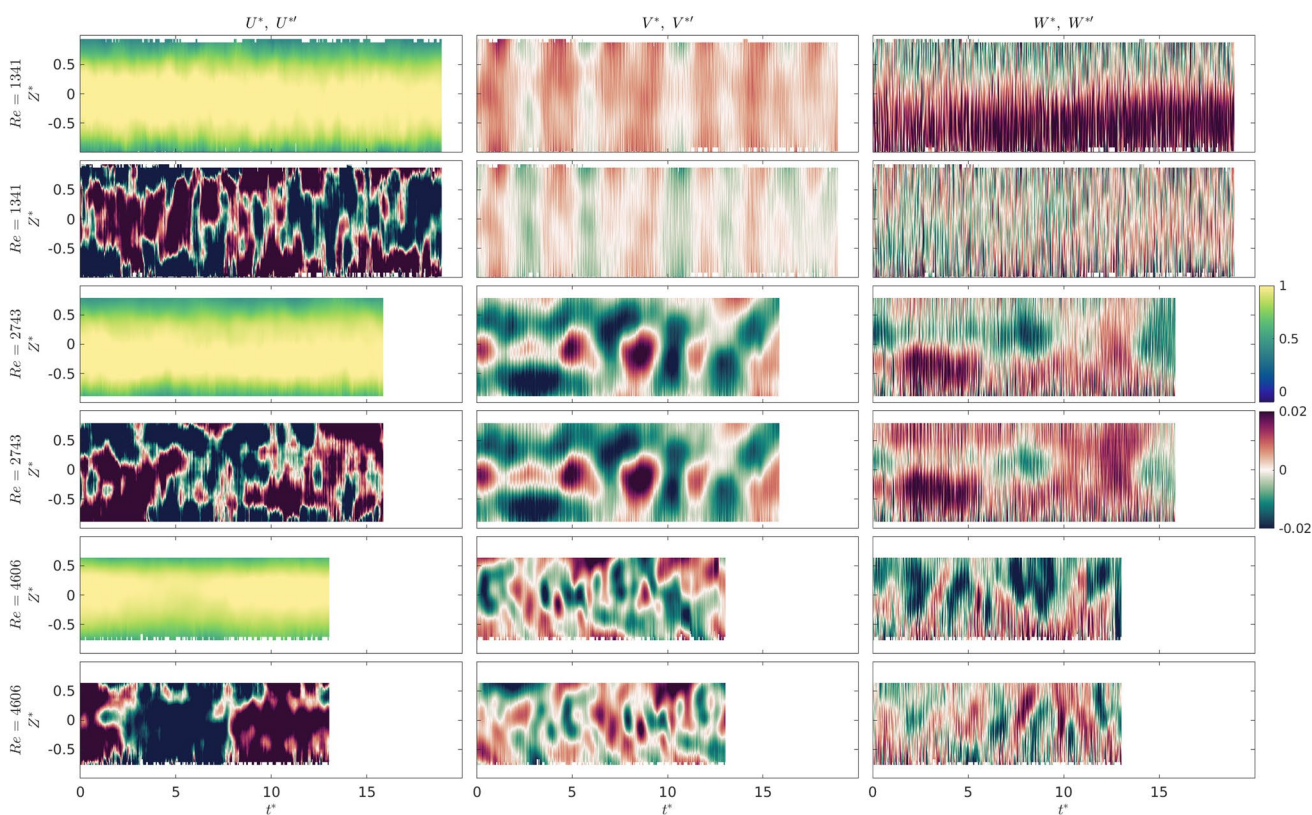


**Fig. 9** (left) Downstream, (centre) vertical, and (right) cross-stream velocities and velocity fluctuations from the mean (calculated by averaging over all body timesteps) at $Y^* = 0$. Each pair of rows corresponds to a particular Reynolds number case, with the upper row being $U^*$, $V^*$, and $W^*$ and the lower row being $U^{*\prime}$, $V^{*\prime}$, and $W^{*\prime}$

## 3.3 The three-dimensional structure of coherent motions

Dynamic mode decomposition (Schmid 2010; Tu et al. 2014; Kou and Zhang 2017) is performed on all three components of velocity in the entire volume simultaneously to give a three-dimensional representation of the coherent structures. As in Marshall et al. (2021b), all velocity components and timesteps are combined into a single matrix such that dynamic mode decomposition is applied to all data

simultaneously. In order for this to be computationally realistic, the dimensionality of the data must be reduced. Therefore, the data are cropped to just above the current height and alternating downstream locations are discarded. Singular value decomposition is carried out using the MATLAB `svd` function with the 'econ' parameter (to further reduce computational data dimensionality) (MATLAB 2020). To carry out dynamic mode decomposition using the MATLAB functions selected, there cannot be any missing data points. In the Re = 2743 and Re = 4606 cases, the vast majority of missing data are at the edges of the illuminated volume. As this can be rectified by removing the edge rows or columns with missing data, with small gaps internal to the measurement region filled in using linear interpolation through the MATLAB `interp` function (MATLAB 2020), frequency analysis is applied to these two cases and not the Re = 1341 case. This lower Reynolds number case has more experimental noise, particularly in the cross-stream velocity measurements, and more missing data (possibly as a result of less even distribution of the seeding particles, a greater difference in refractive index between the fluids, or less optimal timestep or reconstruction settings).

As in Marshall et al. (2021b), the modes with significant contribution to the flow are identified using a combination of Fourier transform, wavelet decomposition, and dynamic mode amplitude. Figure 10 shows the amplitudes of the dynamic modes, and Figs. 11 and 12 show the Fourier transform and wavelet decomposition of the velocity data. The Fourier transform is performed over time both on data at central downstream and cross-stream locations, and at a central downstream location and the height of the velocity maximum. The wavelet decomposition is performed on data at a central downstream and cross-stream location, and at both the height of the velocity maximum and the height of

maximum negative shear. Combining the FFT, wavelet, and dynamic mode amplitude plots, the frequencies of motions with significant impact on the flow, their vertical position within the flow, and the time scales over which they affect the flow can be identified.

Figure 11 identifies a mode with frequency 0.40Hz in the Re = 2743 case. This mode is primarily seen in the vertical velocity plots, above the height of the downstream velocity maximum (around the height of maximum negative shear). The motion is concentrated in the cross-stream centre of the domain but extends throughout the domain width, and is present throughout the flow duration. The Re = 4606 case contains a broader range of frequencies, and frequencies with significant cross-stream FFT amplitude. In particular, a mode with frequency 0.80Hz is identified. Again, this mode is at the height of the velocity maximum and concentrated in the cross-stream centre of the flow. However, the motions extend less far in the cross-stream direction and unlike the 0.40Hz mode, it is seen equally in the downstream and cross-stream FFT and becomes more significant in the wavelet decomposition over time.

Visualisation of the dynamic modes illuminates the structure of the dominant motions for each case. Figures 13 and 14 illustrate the downstream, vertical, and cross-stream motions associated with a mode at each Reynolds number. The other dynamic modes from each case have similar structure. In both cases, the dynamic mode shows motions at the expected position within the flow. For the Re = 2743 mode, the vertical velocities extend further across the domain width than the Re = 4606 mode. Considering the velocity streamlines, the Re = 4606 mode is associated with full-width three-dimensional coherent motions (i.e. motions with equivalent magnitude in the cross-stream and vertical directions) not clearly visible in the Re = 2743



**Fig. 10** Dynamic mode amplitudes for the (left) Re = 2743, and (right) Re = 4606 cases, with red circles to highlight the modes illustrated later in the work

(a)



(b)
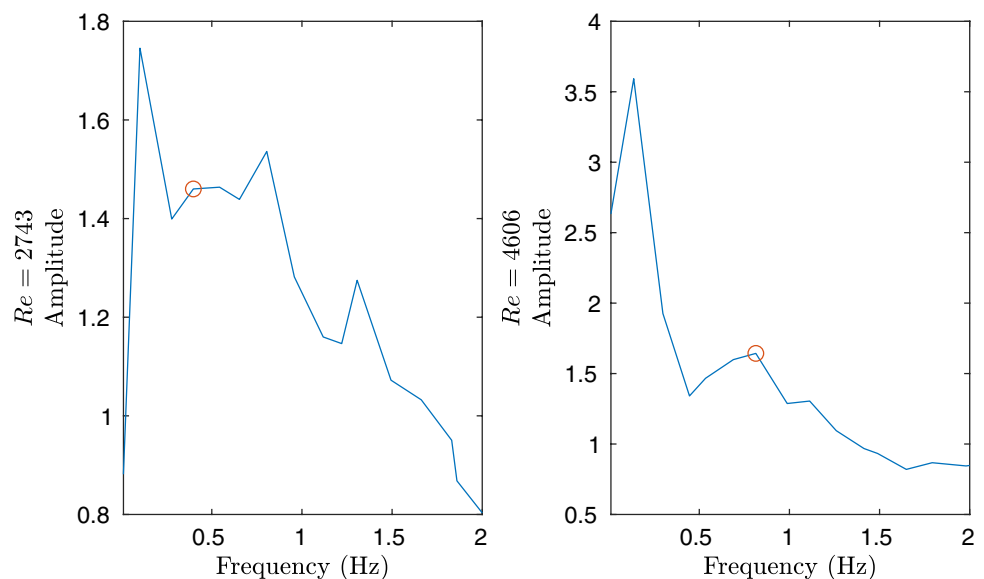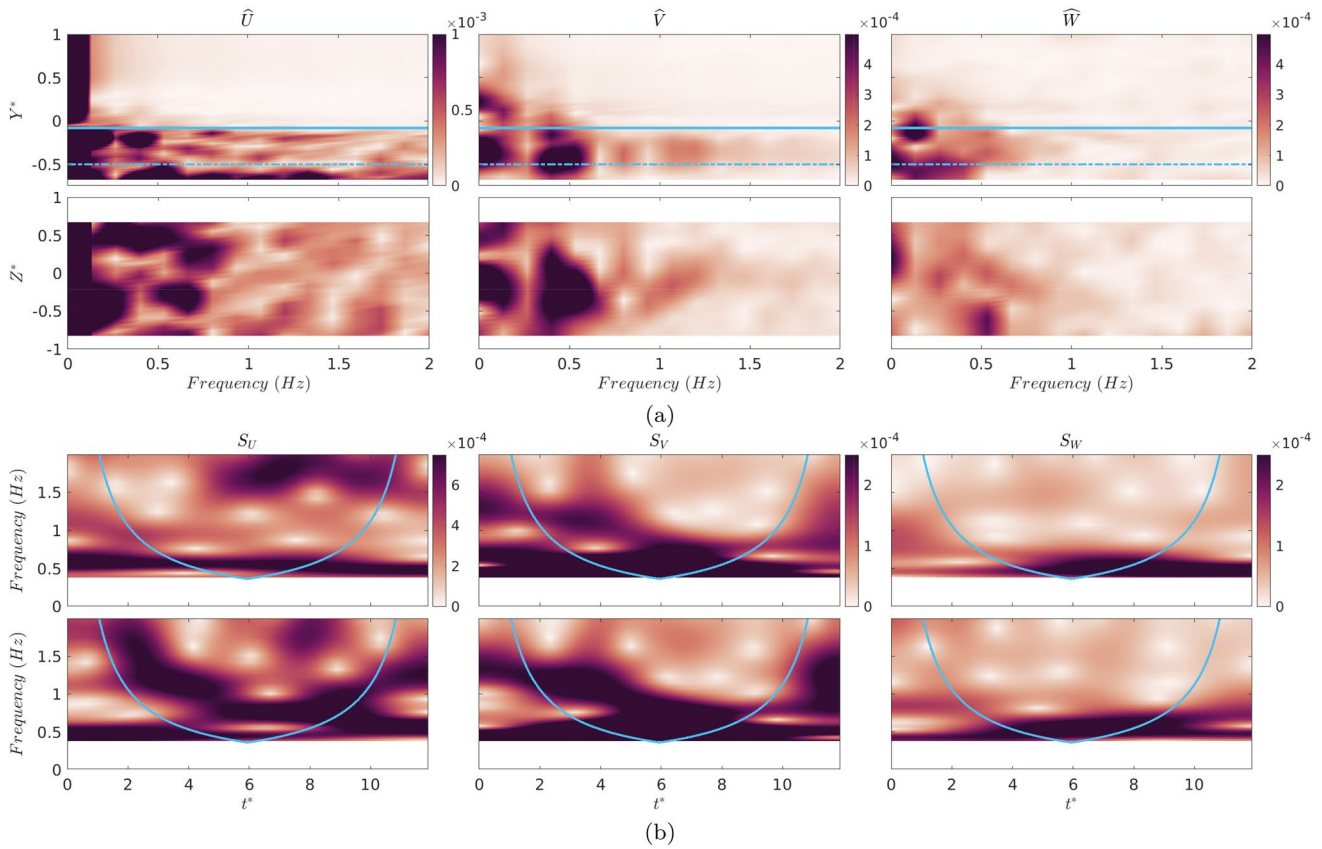
**Fig. 11** Plots of data from the Re = 2743 case: **a** FFT of downstream, vertical, and cross-stream velocities (top) at a central cross-stream and downstream location and (bottom) at a central downstream location and the height of the downstream velocity maximum, and **b** wavelet transform of velocity components at a central cross-stream and downstream location and (top) the height of the velocity maximum, and (bottom) the height of maximum negative shear. The blue lines in (**b**) represent the 'cone of influence' of the wavelet spectrum

mode streamlines. The downstream and vertical velocities on the central cross-stream slice have very similar structure to those modes identified in the planar PIV data (Marshall et al. (2021b)), suggesting that similar motions are being identified in both data sets.

In order to establish whether these motions are due to gravity, as in Marshall et al. (2021b) a heuristic estimate of the Brunt–Väisälä frequency is obtained,

$$N \approx \sqrt{-\frac{g}{\rho_0}\frac{d\overline{\rho}}{dY}}, \qquad (4)$$

where $g$ is the acceleration due to gravity, $\overline{\rho}$ is the average density profile, and $\rho_0$ is taken to be the mean of the glycerol and KDP densities. The average density profile is estimated as in Marshall et al. (2021b). Specifically, excess density ($\rho_e = \rho - \rho_a$, where $\rho_e$ is the excess density, and $\rho_a = 1012 \mathrm{kg\,m^{-3}}$ is the density of the ambient fluid) is estimated to be constant both above the current height (where $\rho_e = 0$ is assumed) and below the velocity maximum (where $\rho_e$ is estimated by requiring conservation of excess density

flux between the inlet and the data) with a linear distribution between the two. Inlet density flux ($F_I$) is estimated by multiplying fluid influx and the excess density of the dense fluid. In order to maintain comparability between this work and that in Marshall et al. (2021b), the excess density flux from the data ($F_e$) is estimated by considering the downstream velocity and density profiles only on a central cross-stream plane,

$$F_e = W_T \int \overline{\rho}\,\overline{U}^{Z^*=0}\mathrm{d}Y, \qquad (5)$$

where $W_T$ is the width of the tank. Excess density below the velocity maximum is estimated by requiring $F_I = F_e$ (Table 5).

The Brunt–Väisälä frequency, $N$, is the upper bound on the angular frequency of internal waves due to buoyancy. A Doppler shift due to the mean flow must be applied,

$$N_{DS} = N + U_0\boldsymbol{k}, \qquad (6)$$
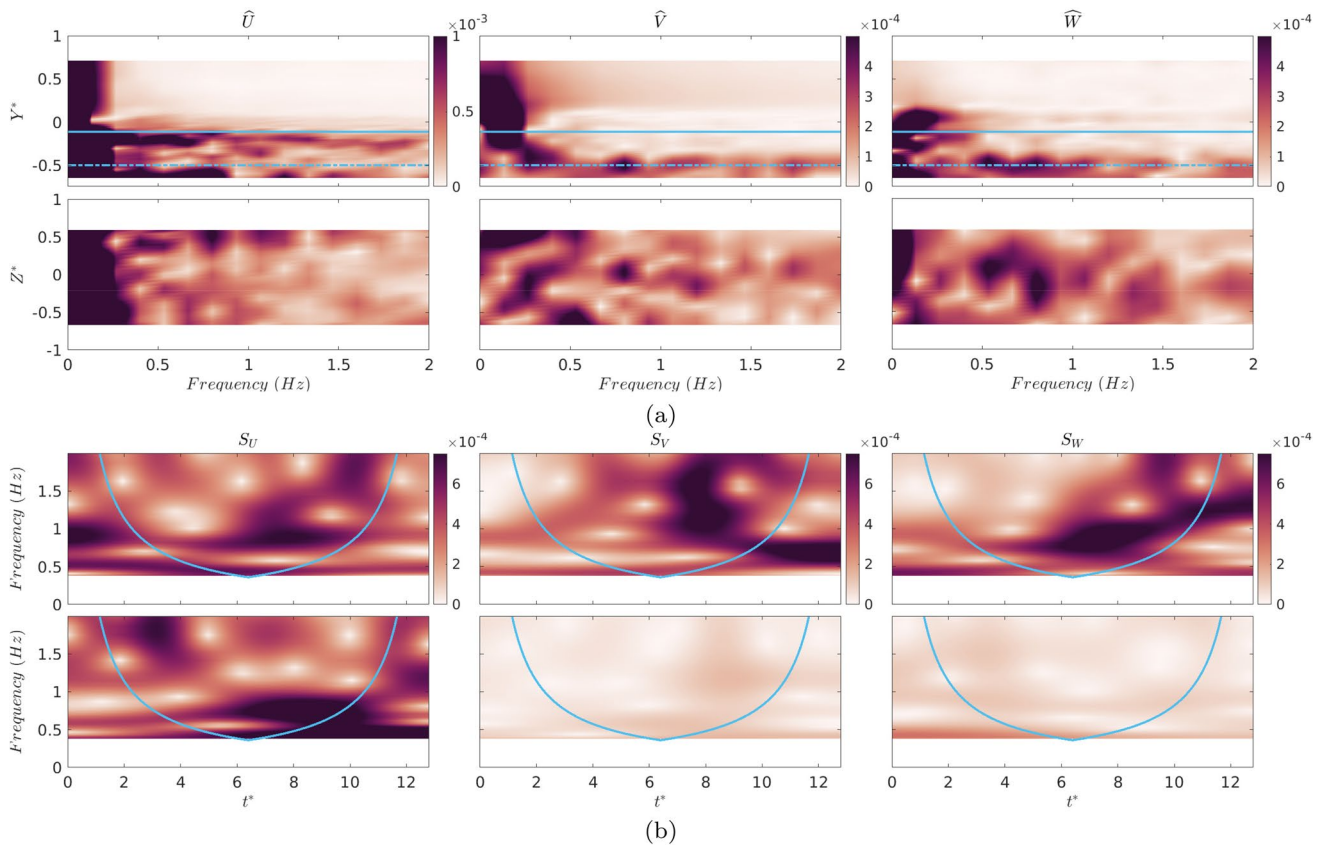
**Fig. 12** Plots of data from the Re = 4606 case: **a** FFT of downstream, vertical, and cross-stream velocities (top) at a central cross-stream and vertical location and (bottom) at a central downstream location and the height of the velocity maximum, and **b** wavelet transform of velocity components at a central cross-stream and downstream location and (top) the height of the velocity maximum, and (bottom) the height of maximum negative shear. The blue lines in (**b**) represent the 'cone of influence' of the wavelet spectrum

where $N_{DS}$ is the frequency measured by a stationary observer, $U_0$ is the mean flow at the height of the wave, and **k** the wavenumber, which is here taken to be the downstream wavenumber $k_x$ as all observed waves propagate downstream. Details of the frequency, wavelength (estimated by inspecting the velocities in Figs. 13 and 14), wave speed, and Doppler shifted buoyancy frequency for each mode are shown in Table 6, along with a comparison of the measured frequency and the upper limit on the expected mode frequency and the wave speed and measured flow speed at the height of the wave. For the Re = 2743 case, the mode height is above the velocity maximum (here estimated to be the height of maximum negative shear, though this is subjective), while the Re = 4606 waves are at the height of the velocity maximum. Given that the density profile is estimated rather than observed, and the wavelengths are approximated by inspecting mode plots such as Figs. 13 and 14, the observed frequencies for all cases are on the right order of magnitude for the modes to be considered internal waves due to gravity. Additionally, given the approximations involved in the wave height and mode wavelength, the estimated wave speed is

very close to the measured flow speed at the height of the wave. This indicates the possible presence of a critical layer in the flow at the height of the velocity maximum.

## 4 Discussion

The data presented calls into question some commonly made assumptions about the structure of the gravity current body, for example, suggesting that a single plane might not be sufficient to fully characterise the flow. As shown in Fig. 9, this is particularly true of the cross-stream centreline (used in, for example, Islam and Imran (2010); Marshall et al. (2021b); Gray et al. (2006)), which is not representative of the flow in general and the cross-stream velocity in particular (especially in the lowest Reynolds number case). The level of cross-stream variations in the flow (as shown in Fig. 9) suggests that even selecting a non-central plane is not sufficient to understand body structure, being unable to capture, for example, the cross-stream motions associated with structures present in the highest Reynolds number case

(a)



(b)                                    (c)                                    (d)
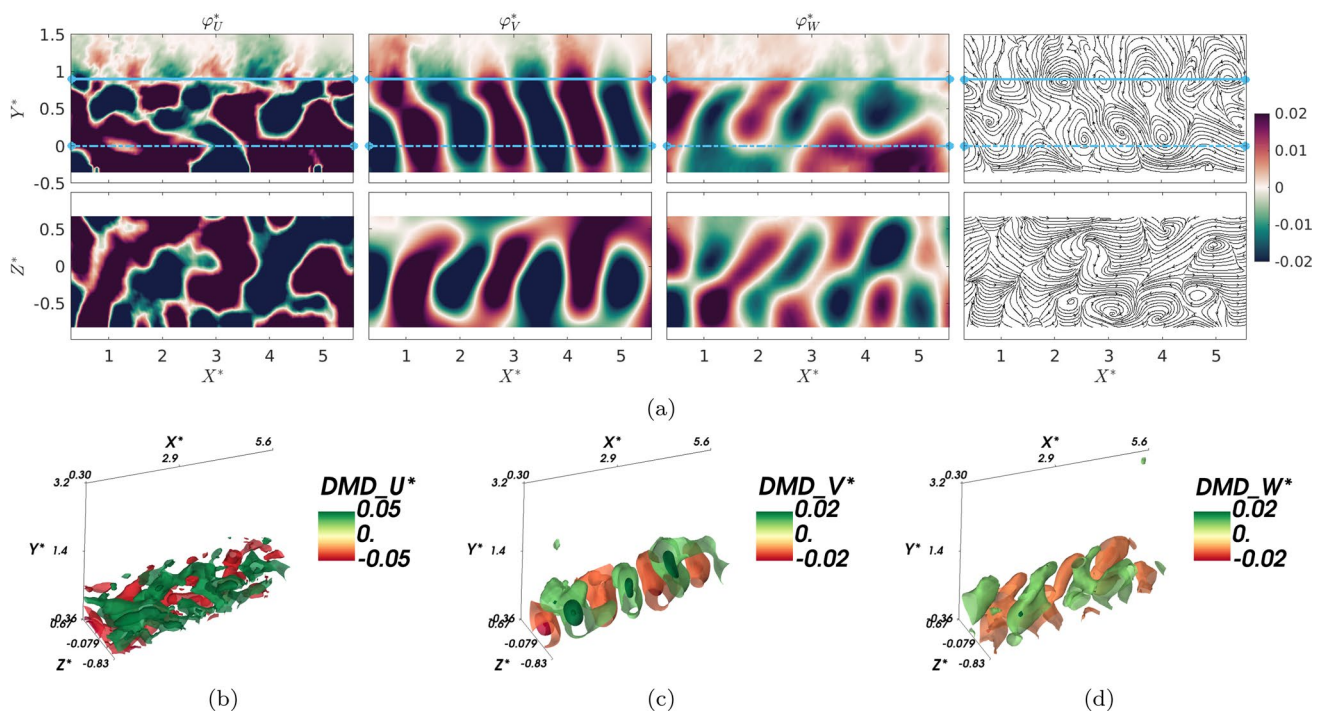
**Fig. 13** **a** Slices showing the structure of (left) downstream, (left-centre) vertical, (centre-right) cross-stream velocities, and (right) two-dimensional velocity streamlines on (top) a central cross-stream slice, and (bottom) a slice at $Y^* = 0.3$ for a mode from the Re = 2743 case with frequency 0.40Hz, and three-dimensional isocontours of **b** the downstream, **c** vertical, and **d** cross-stream velocities associated with this mode



(a)



(b)                                    (c)                                    (d)
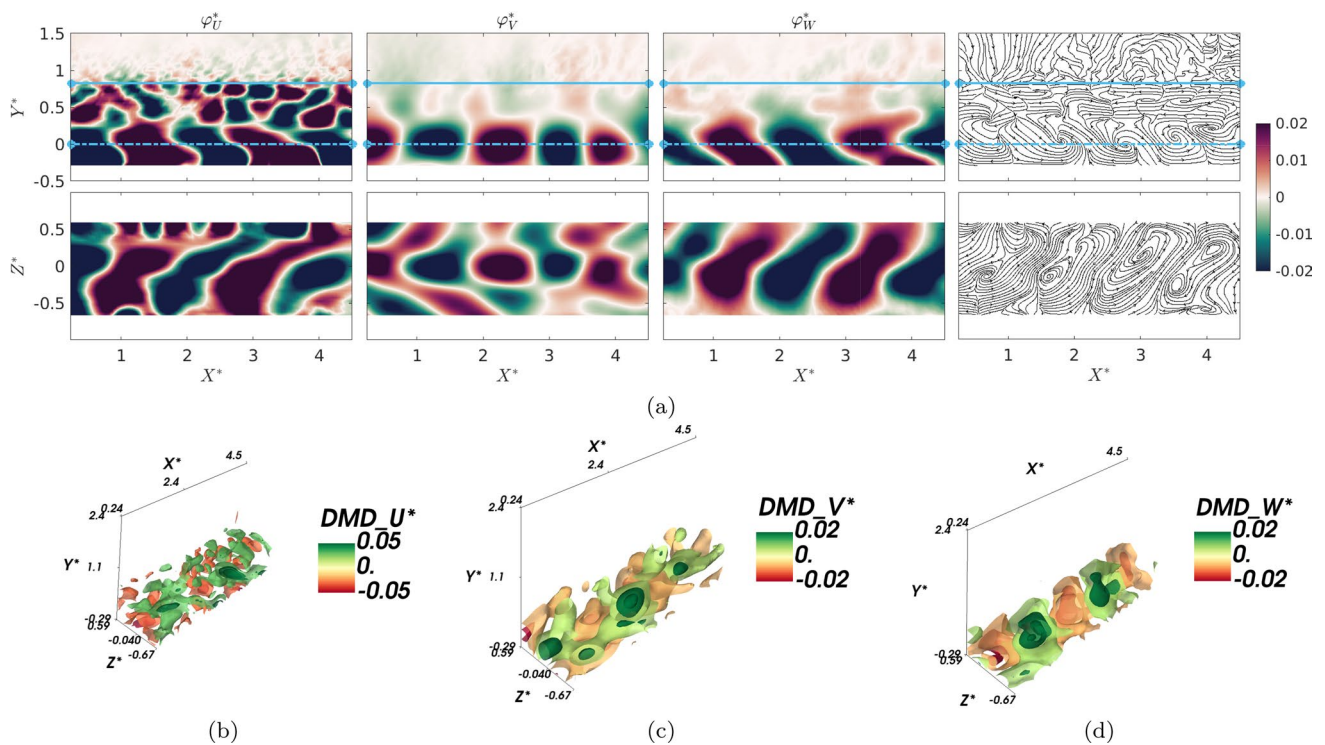
**Fig. 14** **a** Slices showing the structure of (left) downstream, (left-centre) vertical, (centre-right) cross-stream velocities, and (right) two-dimensional velocity streamlines on (top) a central cross-stream slice, and (bottom) a slice at $Y^* = 0$ for a mode from the Re = 4606 case with frequency 0.81Hz, and three-dimensional isocontours of **b** the downstream, **c** vertical, and **d** cross-stream velocities associated with this mode

**Table 5** Details of the inlet excess density flux $F_I$ calculated by taking the product of the fluid influx and the excess density of the KDP, and the estimated maximum excess density within the body calculated by requiring $F_I = F_e$ (where $F_e$ is defined in (5))

| | | |
|---|---|---|
| $Q$ (L s$^{-1}$) | 0.082 | 0.148 |
| $F_I$ (kg s$^{-1}$) | 0.0024 | 0.0044 |
| $\overline{\rho}_e^{\,max}$ (kg m$^{-3}$) | 13.5 | 14.0 |

(Figs. 12 and 14). While concerns around cross-stream centreline data could be linked to the relatively narrow domain of this work, the aspect ratio of the presented currents is comparable with that of previous works quantifying velocity structure in the current body (Islam and Imran 2010; Gray et al. 2006; Cossu and Wells 2012). When investigating these flows, it is therefore advisable to consider if not volumetric measurements then at least multiple planes.

Similarly, there are temporal and spatial (including cross-stream) variations in the velocity and turbulent kinetic energy data (as shown in Figs. 4, 6, and 9), suggesting that averaged values are not sufficient to fully characterise the body. These variations echo the velocity and density variations observed in Marshall et al. (2021b, 2021a) and demonstrate averaging risks underestimating the importance of some parameters, for example, fluctuations in cross-stream velocity, and overlooking features with significant implications for flow dynamics, for example, internal wave-like structures. Additionally, the presented data suggest that cross-stream flow should not be neglected when discussing the gravity current body. While the alternating positive/negative regions of vertical and cross-stream velocities lead to small averaged values, the magnitudes of instantaneous vertical and cross-stream velocity and velocity fluctuations are significant and equivalent (Figs. 5, 8, and 9). Vertical and cross-stream velocities therefore have significant and equivalent contribution to the calculation of turbulent kinetic energy. Crucially the significance of cross-stream velocity fluctuations varies as a function of height, being most prominent at the height of the velocity maximum (as shown in Fig. 6a). At this height, the contribution of cross-stream velocity to turbulent kinetic energy is equivalent in magnitude to

the contributions of downstream and vertical velocities combined.

It has previously been recognised that the height of the downstream velocity maximum is associated with a local minimum of turbulent kinetic energy when only two velocity components are considered (Buckee et al. 2001) (also evident in the data presented here, Fig. 6a). In Buckee et al. (2001), it was suggested that this low level of turbulent kinetic energy, combined with strong stratification, could cause a slow diffusion zone. This would slow mass transport both within the lower part of the current and across the velocity maximum, explaining observed stepped density profiles (Buckee et al. 2001; Ellison and Turner 1959; Garcia and Parker 1993). However, the data presented here highlight that when the third velocity component is taken into account, the level of turbulent kinetic energy at the height of the downstream velocity maximum rises significantly (Fig. 6a). Therefore, an alternative explanation is needed for the observed stepped profiles. Here, we propose internal waves interacting with a critical layer.

Fourier transforms, wavelet transforms, and dynamic mode decomposition (Figs. 11, 12, 13, and 14) have been used to quantify structures in the body of gravity current flows. Excepting the lowest Reynolds number case here, the gravity current body has been shown to contain wave-like structures. These are similar to those observed in Marshall et al. (2021b) (hypothesised to be internal gravity waves, a suggestion supported by the $1/4-$wavelength offset between velocity and density fluctuations observed by Marshall et al. (2021a)) with the same changes in these waves as Reynolds number is increased (namely wave frequency increases, and wave position moves towards the velocity maximum). Peaks in the FFT data suggest that the waves identified in the Re = 2743 case are primarily associated with downstream and vertical velocity but not cross-stream (Fig. 11). The structure is therefore similar to the largely two-dimensional waves previously observed in the core of stratified plane channel flows (García-Villalba and del Álamo 2011; Zonta and Soldati 2018).

By contrast, the waves identified in the Re = 4606 case are associated with peaks in the FFT of cross-stream velocity

**Table 6** Details of the frequency ($f$), angular frequency ($\omega$), wavelength ($\lambda$), wavenumber ($k_x$), flow velocity at the estimated wave height ($U_0$), estimated Brunt–Väisälä frequency ($N$), Doppler shifted estimated Brunt–Väisälä frequency ($N_{DS}$), the ratio of $\omega$ and $N_{DS}$, the wave speed ($c = f\lambda$), and the ratio of wave speed to mean flow speed at the approximate wave height $c/U_{wave}$ for dynamic modes identified as having a significant impact on the flow

| Re | $f$ (Hz) | $\omega$ (rad s$^{-1}$) | $\lambda$ (m) | $k_x$ (m$^{-1}$) | $U_0$ (m s$^{-1}$) | $N$ (rad s$^{-1}$) | $N_{DS}$ (rad s$^{-1}$) | $\frac{\omega}{N_{DS}}$ | $c$ (m s$^{-1}$) | $\frac{c}{U_0}$ |
|---|---|---|---|---|---|---|---|---|---|---|
| 2743 | 0.40 | 2.51 | 0.086 | 73.06 | 0.0237 | 1.88 | 3.88 | 0.65 | 0.034 | 1.43 |
| 4606 | 0.81 | 5.09 | 0.13 | 48.33 | 0.093 | 1.74 | 6.23 | 0.82 | 0.11 | 1.13 |
| 4606 | 1.11 | 6.99 | 0.10 | 62.83 | 0.093 | 1.74 | 7.58 | 0.92 | 0.11 | 1.19 |

(Fig. 12). The streamlines of dynamic modes from this case reveal coherent motions in all three dimensions (with cross-stream velocities equivalent in magnitude to vertical), with the mode having a corkscrew-like structure (Fig. 14). This cross-stream motion may originate with side-wall effects due to the relatively narrow domain; however, the downstream velocity profiles in Fig. 7 demonstrate that the highest Reynolds number flow (the only case shown to contain motions affecting the cross-stream FFT data) is less affected by side walls than the lower Reynolds number flows. Additionally, real-world flows may also be at least partly constrained in the cross-stream direction (for example, turbidity currents in submarine channels (Peakall and Sumner 2015)). These data have demonstrated that even at the moderate Reynolds numbers considered here the flow is unstable to three-dimensional perturbations. The flow could reasonably be expected to become more three-dimensional as Reynolds number (and hence turbulence) is increased further, whatever the original instability triggering the three-dimensionality (such as the breakdown of Kelvin–Helmholtz structures (Meiburg et al. 2015) or flow over bed structures (Bhaganagar and Pillalamarri 2017)).

The phase speed of the observed waves has been found to be approximately equal to the mean flow speed at the wave height, indicating a critical layer within the body. The presence of a critical layer, combined with the demonstrated three-dimensional motions and cross-stream flow variations, has significant implications for possible flow structure (Marshall et al. 2021b; Dorrell et al. 2019). Wave breaking at the critical layer has the potential to form a barrier to mixing, leading to a stepped density profile, maintaining a larger density difference than expected based on current understanding of body flow, and increasing flow speeds and duration. Additionally, absorption of internal waves at the critical layer could transfer horizontal momentum to the mean flow, increasing downstream velocities over time and suggesting that the assumption of a statistically steady body may not be valid in long-running flows.

## 5 Conclusions

The gravity current body has often been described using averaged properties and investigated through measurements taken at a single cross-stream location. The influence of cross-stream flow has typically been neglected, with few seeking to quantify the magnitude and structure of three-dimensional motions within the body. In this paper, Shake-the-Box particle tracking velocimetry has been used to generate instantaneous, three-dimensional, volumetric measurements of velocity in constant-influx solute-based gravity current flows. The measurements call into question these key assumptions regarding body flow and bring to light structures with significant implications for flow dynamics.

The presented velocity measurements illustrate that cross-stream and vertical velocities (and velocity fluctuations) in the body are equivalent in magnitude. Therefore, cross-stream velocity should not be neglected (particularly at the height of the velocity maximum). Additionally, the flow varies both over time (in some cases with a regular pattern) and in the cross-stream direction. Averaging these properties, or relying on data gathered exclusively at a single cross-stream location (particularly the cross-stream centreline), therefore leads to an inaccurate impression of flow structure. Some of the structures identified in this work, for example, have been shown to be associated with cross-stream motions that would not be captured exclusively using averages or data from a single cross-stream location.

Analysis of the presented velocity data though Fourier transforms, wavelet transforms, and dynamic mode decomposition led to the identification of wave-like structures (some with three-dimensional corkscrew-like motions) within the body that may be forming a critical layer near height of the downstream velocity maximum. The presence of three-dimensional motions is significant, as the potential for internal waves interacting with a critical layer to reinforce an eddy transport barrier (with associated implications such as sharper density profiles, and maintenance of the density difference over larger distances than previously anticipated) requires three-dimensional motions and cross-stream density gradients within the flow. While density measurements were beyond the scope of this investigation, the observed three-dimensional structures suggest that an eddy transport barrier is a possibility (particularly in higher Reynolds number flows).

**Author Contributions** C.M. and G.K. carried out the experiment. C.M. wrote the manuscript with support from R.D, G.K, J.P., and S.T., who were also the supervisors for the PhD project of C.M. that the data were collected for. All authors reviewed the manuscript.

## Declarations

**Ethical approval**  Not applicable.

**Conflict of interest**  All authors declare no conflict of interest.

## References

Alahyari A, Longmire EK (1994) Particle image velocimetry in a variable density flow: application to a dynamically evolving microburst. Exp Fluids 17(6):434–440

Altinakar MS, Graf WH, Hopfinger EJ (1996) Flow structure in turbidity currents. J Hydraul Res 34(5):713–718

Azpiroz-Zabala M, Cartigny MJB, Talling PJ, Parsons DR, Sumner EJ, Clare MA, Simmons SM, Cooper C, Pope EL (2017) Newly recognized turbidity current structure can explain prolonged flushing of submarine canyons. Sci Adv 3(10):e1700200

Balasubramanian S, Zhong Q (2018) Entrainment and mixing in lock-exchange gravity currents using simultaneous velocity-density measurements. Phys Fluids 30(5):056601

Bhaganagar K, Pillalamarri NR (2017) Lock-exchange release density currents over three-dimensional regular roughness elements. J Fluid Mech 832:793

Buckee C, Kneller B, Peakall J (2001) Turbulence structure in steady, solute-driven gravity currents. Particulate gravity currents, pp 173–187

Bühler O (2014) Waves and mean flows, 2nd edn. Cambridge University Press

Cantero MI, Lee JR, Balachandar S, García MH (2007) On the front velocity of gravity currents. J Fluid Mech 586:1–39

Cantero MI, Balachandar S, García MH, Bock D (2008) Turbulent structures in planar gravity currents and their influence on the flow dynamics. J Geophys Res: Oceans 113(C8)

Cossu R, Wells MG (2012) A comparison of the shear stress distribution in the bottom boundary layer of experimental density and turbidity currents. Eur J Mech B Fluids 32:70–79

Dai A, Huang YL (2022) On the merging and splitting processes in the lobe-and-cleft structure at a gravity current head. J Fluid Mech 930:A6. https://doi.org/10.1017/jfm.2021.906

Dorrell RM, Peakall J, Darby SE, Parsons DR, Johnson J, Sumner EJ, Wynn RB, Özsoy E, Tezcan D (2019) Self-sharpening induces jet-like structure in seafloor gravity currents. Nat Commun 10(1):1381

Ellison TH, Turner JS (1959) Turbulent entrainment in stratified flows. J Fluid Mech 6(03):423–448

Espath LFR, Pinto LC, Laizet S, Silvestrini JH (2015) High-fidelity simulations of the lobe-and-cleft structures and the deposition map in particle-driven gravity currents. Phys Fluids 27(5):056604. https://doi.org/10.1063/1.4921191

Garcia M, Parker G (1993) Experiments on the entrainment of sediment into suspension by a dense bottom current. J Geophys Res-All Ser 98:4793–4793

García-Villalba M, del Álamo JC (2011) Turbulence modification by stable stratification in channel flow. Phys Fluids 23(4):045104

Gray TE, Alexander J, Leeder MR (2005) Quantifying velocity and turbulence structure in depositing sustained turbidity currents across breaks in slope. Sedimentology 52(3):467–488

Gray TE, Alexander J, Leeder MR (2006) Longitudinal flow evolution and turbulence structure of dynamically similar, sustained, saline density and turbidity currents. J Geophys Res: Oceans 111(C08015), https://doi.org/10.1029/2005JC003089

Hacker J, Linden PF, Dalziel SB (1996) Mixing in lock-release gravity currents. Dyn Atmos Oceans 24(1):183–195

Hallworth MA, Huppert HE, Phillips JC, Sparks RSJ (1996) Entrainment into two-dimensional and axisymmetric turbulent gravity currents. J Fluid Mech 308:289–311

Haynes WM (2014) CRC handbook of chemistry and physics, 95th edn. CRC Press, Boca Raton

Hogg AJ, Nasr-Azadani MM, Ungarish M, Meiburg E (2016) Sustained gravity currents in a channel. J Fluid Mech 798:853–888

Islam MA, Imran J (2010) Vertical structure of continuous release saline and turbidity currents. J Geophys Res: Oceans 115(C08025). https://doi.org/10.1029/2009JC005365

Khripounoff A, Vangriesheim A, Babonneau N, Crassous P, Dennielou B, Savoye B (2003) Direct observation of intense turbidity current activity in the Zaire submarine valley at 4000 m water depth. Mar Geol 194(3–4):151–158

Kneller B, Buckee C (2000) The structure and fluid mechanics of turbidity currents: a review of some recent studies and their geological implications. Sedimentology 47:62–94

Kneller B, Nasr-Azadani MM, Radhakrishnan S, Meiburg E (2016) Long-range sediment transport in the world's oceans by stably stratified turbidity currents. J Geophys Res: Oceans 121(12):8608–8620

Kneller BC, Bennett SJ, McCaffrey WD (1997) Velocity and turbulence structure of density currents and internal solitary waves: potential sediment transport and the formation of wave ripples in deep water. Sed Geol 112(3):235–250

Kneller BC, Bennett SJ, McCaffrey WD (1999) Velocity structure, turbulence and fluid stresses in experimental gravity currents. J Geophys Res 104(C3):5381–5391

Kou J, Zhang W (2017) An improved criterion to select dominant modes from dynamic mode decomposition. Eur J Mech B Fluids 62:109–129

Krug D, Holzner M, Lüthi B, Wolf M, Kinzelbach W, Tsinober A (2015) The turbulent/non-turbulent interface in an inclined dense gravity current. J Fluid Mech 765:303–324

Lefauve A, Partridge JL, Zhou Q, Dalziel SB, Caulfield CP, Linden PF (2018) The structure and origin of confined Holmboe waves. J Fluid Mech 848:508–544

Lowe RJ, Linden PF, Rottman JW (2002) A laboratory study of the velocity structure in an intrusive gravity current. J Fluid Mech 456:33

Marshall C, Dorrell R, Dutta S, Keevil G, Peakall J, Tobias S (2021a) The effect of schmidt number on gravity current flows: The formation of large-scale three-dimensional structures. Phys Fluids 33(10):106601

Marshall C, Dorrell R, Keevil G, Peakall J, Tobias S (2021b) Observations of large-scale coherent structures in gravity currents: implications for flow dynamics. Exp Fluids 62(6):120

MATLAB (2020) 9.8.0.1396136 (R2020a). The MathWorks Inc., Natick, Massachusetts

Meiburg E, Radhakrishnan S, Nasr-Azadani M (2015) Modeling gravity and turbidity currents: computational approaches and challenges. Appl Mech Rev 67(4):040802

Middleton GV (1966) Experiments on Density and Turbidity Currents: I. Motion of the Head. Can J Earth Sci 3(4):523–546

Nasr-Azadani MM, Meiburg E (2014) Turbidity currents interacting with three-dimensional seafloor topography. J Fluid Mech 745:409

Neamtu-Halic MM, Krug D, Haller G, Holzner M (2019) Lagrangian coherent structures and entrainment near the turbulent/non-turbulent interface of a gravity current. J Fluid Mech 877:824–843

Özgökmen TM, Fischer PF, Duan J, Iliescu T (2004) Three-dimensional turbulent bottom density currents from a high-order nonhydrostatic spectral element model. J Phys Oceanogr 34(9):2006–2026

Özsoy E, Di Iorio D, Gregg MC, Backhaus JO (2001) Mixing in the Bosphorus Strait and the Black Sea continental shelf: observations and a model of the dense water outflow. J Mar Syst 31(1–3):99–135

Paik J, Eghbalzadeh A, Sotiropoulos F (2009) Three-dimensional unsteady RANS modeling of discontinuous gravity currents in rectangular domains. J Hydraul Eng 135(6):505–521

Parsons JD, Friedrichs CT, Traykovski PA, Mohrig D, Imran J, Syvitski JPM, Parker G, Puig P, Buttles JL, García MH (2007) The mechanics of marine sediment gravity flows. In: Nittrouer CA, Austin JA, Field ME, Kravitz JH, Syvitski JPM, Wiberg PL (eds) Continental margin sedimentation: from sediment transport to sequence stratigraphy. Blackwell, Oxford, pp 275–333

Peakall J, Sumner EJ (2015) Submarine channel flow processes and deposits: a process-product perspective. Geomorphology 244:95–120

Pelmard J, Norris S, Friedrich H (2020) Statistical characterisation of turbulence for an unsteady gravity current. J Fluid Mech 901:A7

Salinas JS, Balachandar S, Cantero M (2021) Control of turbulent transport in supercritical currents by three families of hairpin vortices. Phys Rev Fluids 6(6):063801

Schanz D, Schröder A, Gesemann S, Michaelis D, Wieneke B (2013) 'Shake The Box': A highly efficient and accurate Tomographic Particle Tracking Velocimetry (TOMO-PTV) method using prediction of particle positions. In: 10th International Symposium on Particle Image Velocimetry

Schanz D, Schröder A, Gesemann S, Wieneke B (2015) 'Shake the box': Lagrangian particle tracking in densely seeded flows at high spatial resolution. In: 9th International Symposium On Turbulence and Shear Flow Phenomena

Schanz D, Gesemann S, Schröder A (2016) Shake-The-Box: Lagrangian particle tracking at high particle image densities. Exp Fluids 57(5):70

Schmid PJ (2010) Dynamic mode decomposition of numerical and experimental data. J Fluid Mech 656:5–28

Sequeiros OE, Spinewine B, Beaubouef RT, Sun T, García MH, Parker G (2010) Characteristics of Velocity and Excess Density Profiles of Saline Underflows and Turbidity Currents Flowing over a Mobile Bed. J Hydraul Eng 136(7):412–433

Simpson JE (1997) Gravity Currents: In the Environment and the Laboratory. Cambridge University Press

Stacey MW, Bowen AJ (1988) The vertical structure of density and turbidity currents: Theory and observations. Journal of Geophysical Research: Oceans 93(C4):3528–3542. https://doi.org/10.1029/JC093iC04p03528

Sumner EJ, Peakall J, Dorrell RM, Parsons DR, Darby SE, Wynn RB, McPhail SD, Perrett J, Webb A, White D (2014) Driven around the bend: Spatial evolution and controls on the orientation of helical bend flow in a natural submarine gravity current. Journal of Geophysical Research: Oceans 119(2):898–913

Tan S, Salibindla A, Masuk AUM, Ni R (2019) An open-source Shake-the-Box method and its performance evaluation. In: 13th International Symposium on Particle Image Velocimetry

Tu JH, Rowley CW, Luchtenburg DM, Brunton SL, Kutz JN (2014) On dynamic mode decomposition: Theory and applications. Journal of Computational Dynamics 1(2):391–421

Ungarish M (2009) An Introduction to Gravity Currents and Intrusions. Chapman and Hall/CRC

Wells MG, Dorrell RM (2021) Turbulence Processes Within Turbidity Currents. Annu Rev Fluid Mech 53:59–83

Wieneke B (2012) Iterative reconstruction of volumetric particle distribution. Meas Sci Technol 24(2):024008

Zonta F, Soldati A (2018) Stably stratified wall-bounded turbulence. Applied Mechanics Reviews 70(4)